Computer Physics Communications 257 (2020) 107510

Contents lists available at ScienceDirect

Computer Physics Communications

journal homepage: www.elsevier.com/locate/cpc

# Numerical evaluation of Sommerfeld-type integrals for reflection and transmission of dipole radiation☆,☆☆

Henk F. Arnoldus

*Department of Physics and Astronomy, Mississippi State University, P.O. Box 5167, Mississippi State, MS 39762, USA*

ARTICLE INFO

*Article history:*
Received 10 January 2020
Received in revised form 24 June 2020
Accepted 13 July 2020
Available online 28 July 2020

*Keywords:*
Electric dipole radiation
Interface
Sommerfeld-type integrals
Traveling and evanescent waves
Poynting vector

ABSTRACT

A radiating electric dipole is located near the interface with a layer of material. The electric and magnetic fields reflect off the interface and transmit through the material. The exact solution of Maxwell's equations can be found in terms of Sommerfeld-type integrals. These integrals have in general a singularity on the integration axis, and the integrands are extremely complicated functions of the parameters in the problem. We present a method for the computation of these integrals, and the corresponding electric and magnetic fields. Key to the solution is the splitting of the incident field in its traveling and evanescent contributions. With a change of variables, the singularities can be transformed away, and the method also greatly improves the accuracy and efficiency of the integration. We illustrate the feasibility of our approach with the computation of the flow lines of electromagnetic energy in the system. For such flow diagrams, a large number of integrals needs to be computed with reasonable accuracy. We show that in our approach even the smallest details in flow diagrams can be revealed.

**Program summary**

*Program titles*: CPiP-Auxiliary-1, CPiP-Auxiliary-2, CPiP-Field lines-1, CPiP-Field lines-2.
*CPC Library link to program files:* http://dx.doi.org/10.17632/476n5ffkvv.1
*Licensing provisions*: GPLv3.
*Programming language*: Mathematica.
*Nature of problem*: In near-field optics and nano-photonics, exact solutions of Maxwell's equations are needed. Of particular interest are the reflected and transmitted electric and magnetic fields of dipole radiation by a layer of material. These solutions involve a large number of integrals, which need to be computed numerically. In the literature, these integrals are known as Sommerfeld-type integrals.
*Solution method*: We split the integration range in two parts. The first part corresponds to traveling dipole waves and the second part results from evanescent dipole waves. In each region we make a (different) change of variables. The result of this transformation is that it removes a possible singularity on the integration axis, and it also has a tendency to smoothen out the integrand. There are 38 different types of integrals. Our method applies to all of them, and is self-contained. There is no need for tweaking of the programs for each of these, and no adjustments need to be made for different values of the parameters. The method is developed for the near field. For large distances to the source (the far field), asymptotic methods are available, and there would be no need for numerical integration.



## 1. Introduction

The problem of reflection of electric dipole radiation by a material medium has a long history. More than a century ago, Sommerfeld [1] studied the propagation of radio waves near the surface of the Earth. His solutions for the reflected electric and magnetic fields were expressed as integral representations, now known as Sommerfeld-type integrals. The integrands contain a Fresnel reflection coefficient, a Bessel function, an exponential, and a branch point singularity on the positive real axis (the integration axis). In addition, the integrand has branch points in the complex plane that can be near the axis of integration, depending on the parameters, and may have a simple pole (plasmon resonance). Moreover, the argument of the exponential has a branch point, which in general is in the complex plane, but may be on the integration axis. We take the dipole to be located on the $z$ axis, a distance $H$ below the interface. The harmonically oscillating dipole has angular frequency $\omega$, and we shall take the

☆ The review of this paper was arranged by Prof. Hazel Andrew.
☆☆ This paper and its associated computer program are available via the Computer Physics Communication homepage on ScienceDirect (http://www.sciencedirect.com/science/journal/00104655).

*E-mail address:* hfa1@msstate.edu.

https://doi.org/10.1016/j.cpc.2020.107510
0010-4655/

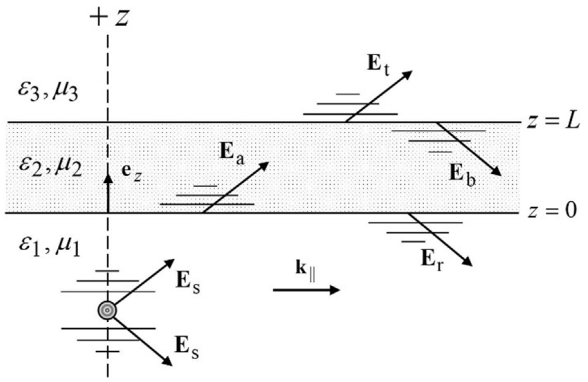


**Fig. 1.** Shown is the dipole near the layer. The arrows indicate the wave vectors of the traveling waves in an angular spectrum representation, and the dashed lines symbolically represent the evanescent waves.

time dependence to be $\exp(-i\omega t)$. The free-space wave number is $k_o = \omega/c$. We shall adopt dimensionless variables in order to reduce the number of parameters. We set $h = k_o H$ for the dimensionless distance between the dipole and the interface. In this way, $2\pi$ corresponds to a free-space optical wavelength. The dimensionless cylindrical coordinates are then $(\overline{\rho}, \phi, \overline{z})$, with $\overline{\rho} = k_o\rho$ and $\overline{z} = k_o z$. The dependence on $\overline{\rho}$ enters only through the arguments of the Bessel functions as $J_n(\alpha\overline{\rho})$, where $\alpha$ is the integration variable, and the range is $0 \leq \alpha < \infty$. Clearly, for $\overline{\rho}$ not too small, the integrand is oscillatory, adding another layer of complexity to the problem. The dependence on $\overline{z}$ enters through the exponential, which is oscillatory for small $\alpha$ and decaying for large $\alpha$. The $\phi$ dependence of the problem comes from the orientation of the oscillating dipole, and enters as factors in the expressions for the fields, but the Sommerfeld-type integrals are independent of $\phi$. The dependence on the wave number $k_o$ only enters as the inverse length scale.

The numerical evaluation of these integrals has been considered by many authors [2–8]. In several approaches, the contour of integration is deformed to a curve in the complex plane in order to avoid branch points. The disadvantage of this method is that the contour depends on the material parameters, in particular the location of the branch points, and needs to be determined on a case-by-case basis. Asymptotic methods have been developed to deal with the oscillatory behavior of the integrands for large $\overline{\rho}$. In this approach, the integral over the tail of the integration region is evaluated analytically with asymptotic methods. Also, clever substitutions have been proposed to smoothen out the fast oscillations.

When the dipole radiation reflects at the interface, part of the radiation is transmitted into the medium. We shall consider the more general setup where the medium is a layer on a substrate, as depicted in Fig. 1. In near-field optics, radiation phenomena on a sub-wavelength scale are of interest. For instance, the dipole energy emission rate depends on the distance $H$ between the dipole and the surface, if this distance is on the order of a wavelength or less [9–11]. With the invention of metamaterials, the very details of the near-field radiation patterns have become of utmost importance. It has been predicted that a thin layer of negative-index-of-refraction material could have the potential to form a sub-wavelength image of a source in region 3 in the figure [12]. Another prediction is that near an epsilon-near-zero metamaterial an electric dipole can levitate in its own reflected field, provided that the particle is very close to the interface [13–16]. In order to understand such phenomena, the electric and magnetic fields must be known with sub-wavelength precision in every of the three regions shown in Fig. 1. The radiation patterns in the far field, either in region 1 or region 3, can be obtained in closed form, for instance with the method of stationary phase [17–19], so we will not be concerned with these far-field limits.

## 2. The setup

We shall consider an electric dipole located near a layer on a substrate, as illustrated in Fig. 1. The lower interface is the $xy$ plane and the second interface is a plane at $z = L$. Each medium is represented by its (relative) permittivity $\varepsilon$ and its (relative) permeability $\mu$. The index of refraction $n$ is then a solution of $n^2 = \varepsilon\mu$, and we take the solution (root) for which the imaginary part of $n$ is positive or zero. For instance, when both $\varepsilon$ and $\mu$ are positive, the index of refraction is $n = \sqrt{\varepsilon\mu}$, and when both $\varepsilon$ and $\mu$ are in the second quadrant of the complex plane we must take the solution $n = -\sqrt{\varepsilon\mu}$. Which solution to take depends on where $\varepsilon$ and $\mu$ are located in the complex plane. To find the correct root, we write $\varepsilon = |\varepsilon|\exp(i\theta_\varepsilon)$, with $0 \leq \theta_\varepsilon \leq \pi$, and similarly for $\mu$. It was shown in [20] that the solutions for the indices of refraction then follow from dividing the phase angles by 2. This is the same as

$$n = \sqrt{\varepsilon}\sqrt{\mu}, \tag{1}$$

when the branch line of the square root function is taken to be just below the negative real axis (as in *Mathematica*). For later purposes we shall take $\varepsilon_1 > 0$, $\mu_1 > 0$, and therefore $n_1 = \sqrt{\varepsilon_1\mu_1} > 0$. The embedding medium of the dipole is transparent.

With the help of Weyl's representation of the scalar Green's function [21], the source field $\mathbf{E}_s$, emitted by the dipole, is represented as a linear superposition of polarized ($s$ and $p$) plane waves. Each wave is either traveling into the direction of the wave vector, as shown by arrows in Fig. 1, or exponentially decaying in the positive $z$ direction, as shown symbolically by the dashed lines. It can also be a combination of both, which happens if $\varepsilon$ or $\mu$ of the medium has an imaginary part. Each plane wave partially reflects at the surface and partially penetrates the layer. Multiple reflections at both interfaces then lead to the $\mathbf{E}_a$ and $\mathbf{E}_b$ waves in the layer. Part of the light exits the layer as the transmitted wave $\mathbf{E}_t$. The complex amplitudes of the various waves, relative to the incident wave, are the Fresnel coefficients for these waves. Their explicit expressions are given in the Appendix. The total reflected (r), layer (a and b), and transmitted (t) waves then follow by making the same superposition as for the incident field.

For any of the wave vectors, the wave number is $k^2 = \varepsilon\mu k_o^2$. All wave vectors in Fig. 1 must have the same parallel component $\mathbf{k}_\parallel$, otherwise the boundary conditions at the interfaces cannot be met. This is used explicitly in the derivation of the Fresnel coefficients. In an angular spectrum representation, this $\mathbf{k}_\parallel$ labels the partial waves, and it is the integration variable for the superposition. The integral runs over the entire $\mathbf{k}_\parallel$ plane, which is the $xy$ plane. For a given $\mathbf{k}_\parallel$ we then have for the $z$ component of a wave vector: $k_z^2 = \varepsilon\mu k_o^2 - k_\parallel^2$, and this gives two possible values for $k_z$. We set $k_z = \pm k_o v$, and we introduce the variable $\alpha$ as

$$\alpha = k_\parallel/k_o. \tag{2}$$

We then get $v^2 = n^2 - \alpha^2$, and this determines the variable $v$, apart from a minus sign. Just like for the index of refraction, we take the solution in the upper half of the complex plane, and possibly on the real axis. Which root to take then depends on the values of $n$ and $\alpha$. It can be shown that if we take

$$v = \sqrt{n+\alpha}\sqrt{n-\alpha}, \tag{3}$$

then this is the correct solution for all possible combinations of parameters. So, we have a $v_1$, a $v_2$ and a $v_3$, which go along with the corresponding indices of refraction $n_1$, $n_2$ and $n_3$. These $v$'s are functions of $\alpha$, and $\alpha$ is in the range $0 \leq \alpha < \infty$. From Fig. 1

we then see that for the incident wave (the $\mathbf{E}_s$ going up) we have $k_{i,z} = k_o v_1$. For the $\mathbf{E}_s$ directed away from the interface and for the r wave, the $z$ components of the wave vectors are $-k_o v_1$. For the a and b waves we have $k_o v_2$ and $-k_o v_2$, respectively, and for the t wave we have $k_{t,z} = k_o v_3$.

The dipole is located on the $z$ axis, a distance $H$ below the lower interface. The dipole moment of the oscillating dipole is in its most general form given by

$$\mathbf{d}(t) = \mathrm{Re}(\mathbf{d}e^{-i\omega t}), \tag{4}$$

where the complex amplitude $\mathbf{d}$ is any complex-valued vector. This vector can be written as

$$\mathbf{d} = d_o\hat{\mathbf{u}},\ d_o > 0,\ \hat{\mathbf{u}}^*\cdot\hat{\mathbf{u}} = 1. \tag{5}$$

The amplitude constant $d_o$ only affects the overall factors in the fields. The complex-valued unit polarization vector determines the state of oscillation. For $\hat{\mathbf{u}}$ real, the dipole oscillates linearly along the $\hat{\mathbf{u}}$ direction, and for $\hat{\mathbf{u}}$ complex the dipole moment $\mathbf{d}(t)$ traces out an ellipse in a plane. By appropriate choice of $\hat{\mathbf{u}}$, this can be any ellipse in any plane [22]. In Sommerfeld's problem, he had $\hat{\mathbf{u}} = \mathbf{e}_z$, corresponding to a dipole oscillating perpendicular to the interface. Another popular choice is $\hat{\mathbf{u}} = \mathbf{e}_y$, which represents a dipole oscillating parallel to the interface. For instance, for

$$\hat{\mathbf{u}} = -\frac{1}{\sqrt{2}}(\mathbf{e}_y + i\mathbf{e}_z), \tag{6}$$

the dipole moment traces out a circle in the $yz$ plane, rotating counterclockwise when viewed down the positive $x$ axis (left-polarized, or positive helicity). We shall make no assumptions about this vector $\hat{\mathbf{u}}$, and consider the general solution which covers all cases.

## 3. Solution in terms of sommerfeld-type integrals

The electric and magnetic fields for the setup depicted in Fig. 1 can be found in closed form. For the electric and magnetic fields, we split off factors as

$$\mathbf{E}(\mathbf{r}) = \mu_1\zeta\tilde{\mathbf{E}}(\mathbf{r}), \tag{7}$$

$$\mathbf{B}(\mathbf{r}) = \mu_1\frac{\zeta}{c}\tilde{\mathbf{B}}(\mathbf{r}), \tag{8}$$

with

$$\zeta = \frac{k_o^3 d_o}{4\pi\varepsilon_o}. \tag{9}$$

In this way, $\tilde{\mathbf{E}}(\mathbf{r})$ and $\tilde{\mathbf{B}}(\mathbf{r})$ are dimensionless, and any dependence on the wave number is contained in the overall constant $\zeta$, apart from the fact that spatial dimensions are measured in inverse wave numbers. We have $h = k_o H$ for the distance between the dipole and the interface, $\ell = k_o L$ for the dimensionless layer thickness, and $\bar{x}$, $\bar{\rho}$, etc. for the various coordinates.

Let $\mathbf{q}_1 = k_o\mathbf{r}_1$ be the dimensionless location of the field point with respect to the location of the dipole. So,

$$\mathbf{q}_1 = \bar{x}\mathbf{e}_x + \bar{y}\mathbf{e}_y + (\bar{z}+h)\mathbf{e}_z\ . \tag{10}$$

For the source field we then have [23]

$$\tilde{\mathbf{E}}_s = \left\{\hat{\mathbf{u}} - (\hat{\mathbf{q}}_1\cdot\hat{\mathbf{u}})\hat{\mathbf{q}}_1 + \left[\hat{\mathbf{u}} - 3(\hat{\mathbf{q}}_1\cdot\hat{\mathbf{u}})\hat{\mathbf{q}}_1\right] \times\frac{i}{n_1q_1}\left(1+\frac{i}{n_1q_1}\right)\right\}\frac{e^{in_1q_1}}{q_1}, \tag{11}$$

$$\tilde{\mathbf{B}}_s = n_1(\hat{\mathbf{q}}_1\times\hat{\mathbf{u}})\left(1+\frac{i}{n_1q_1}\right)\frac{e^{in_1q_1}}{q_1}, \tag{12}$$

with $q_1 = |\mathbf{q}_1|$ and $\hat{\mathbf{q}}_1 = \mathbf{q}_1/q_1$.

Expressions for the fields in regions 1, 2 and 3 are derived in Ref. [24]. We adopt polar coordinates $(\bar{\rho},\phi)$ in the $\bar{x}\bar{y}$ plane, so the unit vectors are

$$\mathbf{e}_\rho = \mathbf{e}_x\cos\phi + \mathbf{e}_y\sin\phi, \tag{13}$$

$$\mathbf{e}_\phi = -\mathbf{e}_x\sin\phi + \mathbf{e}_y\cos\phi. \tag{14}$$

The dependence on the dipole polarization vector $\hat{\mathbf{u}}$ enters only through its cylindrical coordinates components $u_\rho = \hat{\mathbf{u}}\cdot\mathbf{e}_\rho$, $u_\phi = \hat{\mathbf{u}}\cdot\mathbf{e}_\phi$ and $u_z = \hat{\mathbf{u}}\cdot\mathbf{e}_z$. The fields are then found to be

$$\tilde{\mathbf{E}}_1 = \tilde{\mathbf{E}}_s + \mathbf{e}_\rho u_\rho(\mathcal{R}_s^{(1)} + \mathcal{R}_p^{(1)}) + \mathbf{e}_\phi u_\phi(\mathcal{R}_s^{(2)} + \mathcal{R}_p^{(2)}) + \mathbf{e}_z u_z\mathcal{R}_p^{(3)} + (\mathbf{e}_\rho u_z - \mathbf{e}_z u_\rho)\mathcal{R}_p^{(4)}, \tag{15}$$

$$\tilde{\mathbf{B}}_1 = \tilde{\mathbf{B}}_s + \mathbf{e}_\rho u_\phi(\mathcal{R}_s^{(3)} + \mathcal{R}_p^{(5)}) + \mathbf{e}_\phi u_\rho(\mathcal{R}_s^{(4)} + \mathcal{R}_p^{(6)}) + \mathbf{e}_z u_\phi\mathcal{R}_s^{(5)} + \mathbf{e}_\phi u_z\mathcal{R}_p^{(7)}, \tag{16}$$

$$\tilde{\mathbf{E}}_2 = \mathbf{e}_\rho u_\rho(\mathcal{L}_s^{(1)} + \mathcal{L}_p^{(1)}) + \mathbf{e}_\phi u_\phi(\mathcal{L}_s^{(2)} + \mathcal{L}_p^{(2)}) + \mathbf{e}_z u_z\mathcal{L}_p^{(3)} + \mathbf{e}_\rho u_z\mathcal{L}_p^{(4)} + \mathbf{e}_z u_\rho\mathcal{L}_p^{(5)}, \tag{17}$$

$$\tilde{\mathbf{B}}_2 = \mathbf{e}_\rho u_\phi(\mathcal{L}_s^{(3)} + \mathcal{L}_p^{(6)}) + \mathbf{e}_\phi u_\rho(\mathcal{L}_s^{(4)} + \mathcal{L}_p^{(7)}) + \mathbf{e}_z u_\phi\mathcal{L}_s^{(5)} + \mathbf{e}_\phi u_z\mathcal{L}_p^{(8)}, \tag{18}$$

$$\tilde{\mathbf{E}}_3 = \mathbf{e}_\rho u_\rho(\mathcal{T}_s^{(1)} + \mathcal{T}_p^{(1)}) + \mathbf{e}_\phi u_\phi(\mathcal{T}_s^{(2)} + \mathcal{T}_p^{(2)}) + \mathbf{e}_z u_z\mathcal{T}_p^{(3)} + \mathbf{e}_\rho u_z\mathcal{T}_p^{(4)} + \mathbf{e}_z u_\rho\mathcal{T}_p^{(5)}, \tag{19}$$

$$\tilde{\mathbf{B}}_3 = \mathbf{e}_\rho u_\phi(\mathcal{T}_s^{(3)} + \mathcal{T}_p^{(6)}) + \mathbf{e}_\phi u_\rho(\mathcal{T}_s^{(4)} + \mathcal{T}_p^{(7)}) + \mathbf{e}_z u_\phi\mathcal{T}_s^{(5)} + \mathbf{e}_\phi u_z\mathcal{T}_p^{(8)}. \tag{20}$$

The functions $\mathcal{R}_\sigma^{(i)}$, $\mathcal{L}_\sigma^{(i)}$ and $\mathcal{T}_\sigma^{(i)}$ are the auxiliary functions needed to construct the fields. Their explicit expressions are given in the Appendix. It should be noted that there is a significant improvement for the representation for fields in the layer, as compared to the results derived in Ref. [24]. These auxiliary functions are Sommerfeld-type integrals, and their numerical evaluation is a challenge. Moreover, for each field point $(\bar{\rho},\phi,\bar{z})$ it requires 12 or 13 of these integrals to be computed in order to find the electric and magnetic field at that single point.

For the special case of a single interface, we set $\ell = 0$. The medium 2 disappears, and there is no need for $\tilde{\mathbf{E}}_2$, $\tilde{\mathbf{B}}_2$, and the auxiliary functions $\mathcal{L}_\sigma^{(i)}$. Also, the remaining auxiliary functions $\mathcal{R}_\sigma^{(i)}$ and $\mathcal{T}_\sigma^{(i)}$ simplify considerably, as shown in the Appendix.

## 4. Auxiliary functions

Let us first consider the function $\mathcal{R}_s^{(1)}$, given by Eq. (A.18), and for a single interface. Written out more explicitly, it reads

$$\mathcal{R}_s^{(1)}(\bar{\rho},\bar{z}) = \frac{i}{2}\int_0^\infty d\alpha\,\frac{\alpha}{v_1(\alpha)}\frac{\mu_3 v_1(\alpha) - \mu_1 v_3(\alpha)}{\mu_3 v_1(\alpha) + \mu_1 v_3(\alpha)}e^{iv_1(\alpha)(h-\bar{z})} \times\left(J_0(\alpha\bar{\rho}) + J_2(\alpha\bar{\rho})\right). \tag{21}$$

Here, $v_1(\alpha)$ and $v_3(\alpha)$ are given by Eq. (3) with $n = n_1$ and $n = n_3$, respectively. To see what we are integrating, the integrand as a function of $\alpha$ is shown in Fig. 2, with the parameters given in the caption. The solid curve is the real part and the dashed curve is the imaginary part of the integrand. The index of refraction of the embedding medium is $n_1$, which is positive. From Eq. (3) we see that for $\alpha = n_1$ we have $v_1 = 0$. This $v_1$ appears in the numerator of the integrand, and therefore we have a singularity at $\alpha = n_1$, as can clearly be seen from the figure. This singularity is on the $\alpha$ axis, the axis of integration. We shall see below that this singularity is integrable.

The integral over $\alpha$ is shown in Fig. 3. The solid and dashed curves are the real and imaginary parts of this auxiliary function. The integration was done with *NIntegrate* in *Mathematica*, and

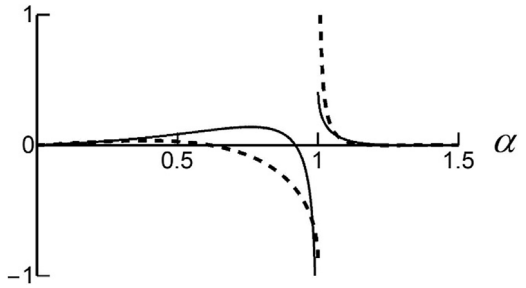


**Fig. 2.** The graph shows the integrand on the right-hand side of Eq. (21) for $\varepsilon_1 = 1$, $\varepsilon_3 = 2$, $\mu_1 = \mu_3 = 1$, $h = 2$, $\overline{\rho} = 3$ and $\overline{z} = -2$.

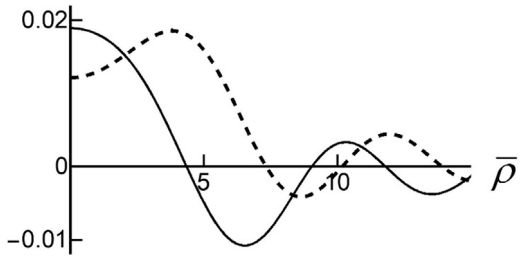


**Fig. 3.** The graph shows the function $\mathcal{R}_s^{(1)}(\overline{\rho},\overline{z})$ from Eq. (21) as a function of $\overline{\rho}$, and for $\overline{z} = -2$. The parameters are the same as for Fig. 2.

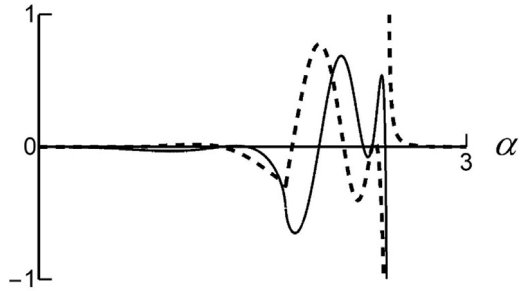


**Fig. 4.** The graph shows the integrand of $\mathcal{R}_s^{(5)}(\overline{\rho},\overline{z})$ for $\varepsilon_1 = 6$, $\varepsilon_3 = 3 + 0.01 * i$, $\mu_1 = \mu_3 = 1$, $h = 2$, $\overline{\rho} = 3$ and $\overline{z} = -2$.

apparently, the singularity is easily handled by the software. Each point of this graph is an integral over $\alpha$. Despite the large number of integrals to be computed for this graph, the runtime is less than one minute. The AccuracyGoal for integrations was set at 6 for this graph, and will be the same for other graphs to follow.

Let us now consider $\mathcal{R}_s^{(5)}$, given by Eq. (A.22), for a single interface, and with the parameters given in the caption of Fig. 4. The index of refraction is $n_1 = 2.45$, and we see again a sharp peak at $\alpha = n_1$. Some other oscillations appear for $\alpha < n_1$. Fig. 5 shows the auxiliary function $\mathcal{R}_s^{(5)}$, obtained by integrating over $\alpha$. The indicated point $\overline{\rho} = 3$ is the integral over the curve in Fig. 4. Even though *Mathematica* does not give convergence warnings, the result is obviously miserable. Moreover, the computation time for the graph in Fig. 5 is 21 min, which is much too slow for any applications.

The integrands of $\mathcal{R}_s^{(1)}$ and $\mathcal{R}_s^{(5)}$ have the $1/v_1$ singularity. For the example with $\mathcal{R}_s^{(1)}$, this appeared to be no problem, whereas for the example with $\mathcal{R}_s^{(5)}$ the numerical integration yielded an unacceptable result.

## 5. Traveling and evanescent integrations

For the embedding medium of the dipole we have $\varepsilon_1 > 0$ and $\mu_1 > 0$, which is the most common case. Then $n_1 > 0$, and $v_1 = 0$

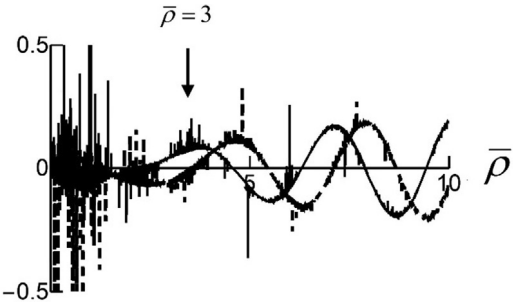


**Fig. 5.** The graph shows the function $\mathcal{R}_s^{(5)}(\overline{\rho},\overline{z})$ as a function of $\overline{\rho}$, and for $\overline{z} = -2$. The parameters are the same as for Fig. 4.

at $\alpha = n_1$. The functions $\mathcal{R}_s^{(1)}$, $\mathcal{R}_s^{(2)}$, $\mathcal{R}_s^{(5)}$, $\mathcal{R}_p^{(3)}$ and $\mathcal{R}_p^{(7)}$ have this $v_1$ in the denominator of the integrand, and therefore there is a singularity on the line of integration. As shown in the previous section, this may or may not be a problem in the numerical integration. Whether this is a problem does not only depend on the function under consideration, but also on the parameters.

In order to resolve this issue of a singularity on the line of integration, we split the integrals over $\alpha$ as follows:

$$\int_0^\infty \mathrm{d}\alpha(\ldots) = \int_0^{n_1} \mathrm{d}\alpha(\ldots) + \int_{n_1}^\infty \mathrm{d}\alpha(\ldots). \tag{22}$$

The separation point of the integrals is at the location of the singularity. The splitting has a physical significance. For the first integral, the integration range is $0 \leq \alpha < n_1$. For these values of $\alpha$, the function $v_1(\alpha)$ is real and positive. Since $k_o v_1$ is the $z$ component of a wave vector in the angular spectrum representation of the incident source field, the corresponding wave vector is real, and therefore this represents a traveling incident wave. For the second integral we have $\alpha > n_1$, and $v_1$ is positive imaginary. The angular spectrum incident plane wave is evanescent, and decays exponentially in the positive $z$ direction. The splitting of the integral in Eq. (22) is a splitting in traveling ($tr$) and evanescent ($ev$) incident waves. We shall write, for instance, $\mathcal{R}_s^{(1)tr}$ and $\mathcal{R}_s^{(1)ev}$ for the respective contributions to this auxiliary function.

For the traveling part we make the change of variables $\alpha \to u$

$$n_1 u = \sqrt{n_1^2 - \alpha^2} \quad (tr). \tag{23}$$

For functions with the $1/v_1$ singularity, we then have

$$\int_0^{n_1} \mathrm{d}\alpha \frac{\alpha}{v_1}(\ldots) = n_1 \int_0^1 \mathrm{d}u(\ldots), \tag{24}$$

and in the new representation on the right-hand side the singularity has disappeared. The other functions have the form

$$\int_0^{n_1} \mathrm{d}\alpha\, \alpha(\ldots) = n_1^2 \int_0^1 \mathrm{d}u\, u(\ldots), \tag{25}$$

and we shall see later that there is an advantage to split these functions as well. The change of variables in Eq. (24) also shows that the singularity in the $\alpha$ representation is integrable from the left.

In the evanescent region we make the change of variables

$$n_1 u = \sqrt{\alpha^2 - n_1^2} \quad (ev). \tag{26}$$

Integrals then transform as

$$\int_{n_1}^\infty \mathrm{d}\alpha \frac{\alpha}{v_1}(\ldots) = -in_1 \int_0^\infty \mathrm{d}u(\ldots), \tag{27}$$

$$\int_{n_1}^\infty \mathrm{d}\alpha\, \alpha(\ldots) = n_1^2 \int_0^\infty \mathrm{d}u\, u(\ldots). \tag{28}$$

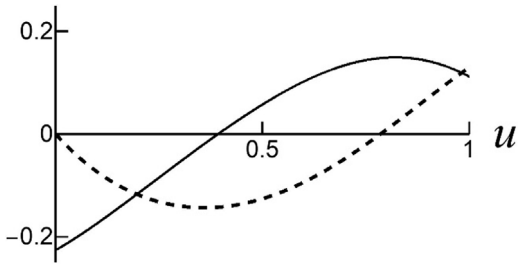


**Fig. 6.** The graph shows the traveling part of the integrand of $\mathcal{R}_s^{(1)}$ for $\varepsilon_1 = 1$, $\varepsilon_3 = 2$, $\mu_1 = \mu_3 = 1$, $h = 2$, $\overline{\rho} = 3$ and $\overline{z} = -2$, as a function of $u$.

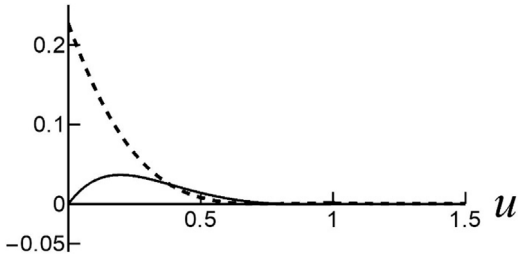


**Fig. 7.** The graph shows the evanescent part of the integrand of $\mathcal{R}_s^{(1)}$ for $\varepsilon_1 = 1$, $\varepsilon_3 = 2$, $\mu_1 = \mu_3 = 1$, $h = 2$, $\overline{\rho} = 3$ and $\overline{z} = -2$, as a function of $u$.

From Eq. (27) it follows that also in the evanescent region the $1/v_1$ singularity has been transformed away, so in the $\alpha$ representation this singularity is also integrable from the right. In both transformations the singular point at $\alpha = n_1$ moves to the point $u = 0$ in the new representation.

In the above transformations, the remaining parts of the integrands have to be written as a function of $u$. This is done by expressing $\alpha$ in terms of $u$ as

$$\alpha = n_1\sqrt{1-u^2}\ (tr), \tag{29}$$

$$\alpha = n_1\sqrt{1+u^2}\ (ev). \tag{30}$$

## 6. Auxiliary functions in the *tr*+*ev* representation

In order to see the advantage of the splitting, we consider the same examples as in Section 4. The integrand of $\mathcal{R}_s^{(1)}$ is shown in Fig. 2 in the $\alpha$ representation. After the transformation we get new integrands, which are now a function of $u$. Fig. 6 shows the traveling part of the integrand, which corresponds to the range $0 \le \alpha < 1$ in Fig. 2. The point $\alpha = 1$ corresponds to the point $u = 0$ in the $u$ representation, and clearly the singularity has disappeared. Fig. 7 shows the transformed evanescent part, corresponding to the range $1 < \alpha < \infty$ in Fig. 2. The lower limit $\alpha = 1$ in Fig. 2 has a singularity, whereas the integrand in the corresponding point $u = 0$ in Fig. 7 is finite.

Next, we consider the integrand of $\mathcal{R}_s^{(5)}$, shown as a function of $\alpha$ in Fig. 4 for a given value of $\overline{\rho}$. The traveling and evanescent parts in the $u$ representation are shown in Figs. 8 and 9, respectively. Both in the traveling and in the evanescent parts, the rapid oscillations near $\alpha = n_1 = 2.45$ have smoothened out considerably. When integrating over $\alpha$ to find the auxiliary function $\mathcal{R}_s^{(5)}$, we obtained the graph in Fig. 5. The result for integration over $u$ is shown in Fig. 10. Whereas the result with the $\alpha$ integration is basically useless, the result with the $u$ integration is perfect. Moreover, the computation time for the graph in Fig. 5 is 21 min, but the graph in Fig. 10 only takes 2 min. It should also be noted that each point in the graphs in Figs. 5 and 10 requires an integration, since the value of $\overline{\rho}$ varies from point to point. So, a large number of integrals needs to be computed to produce these graphs. We conclude that the $tr + ev$ splitting not only greatly improves the accuracy of the integration, but it also reduces the computation time tremendously.

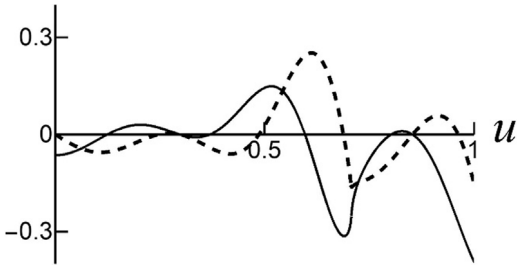


**Fig. 8.** Shown is the traveling part of the integrand of $\mathcal{R}_s^{(5)}$ for the same parameters as in Fig. 4.

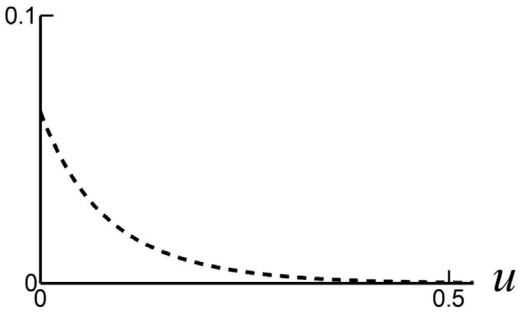


**Fig. 9.** Shown is the evanescent part of the integrand of $\mathcal{R}_s^{(5)}$ for the same parameters as in Fig. 4.

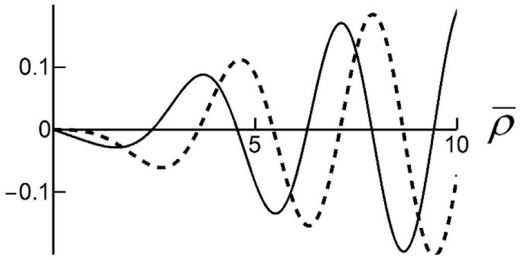


**Fig. 10.** The graph shows the function $\mathcal{R}_s^{(5)}$ as a function of $\overline{\rho}$, and for $\overline{z} = -2$. The parameters are the same as for Fig. 5.

Although the $tr + ev$ splitting and the associated change of variables was mainly introduced to alleviate the numerical integration of integrals with the $1/v_1$ singularity at the index of refraction, there appears to be also an advantage to split the remaining integrals. These are of the form shown in Eqs. (25) and (28). We recall that the point $\alpha = n_1$ becomes the point $u = 0$ for both the traveling and the evanescent integrals. We see from Eqs. (25) and (28) that the integrands in the $u$ representation pick up a factor of $u$. Therefore, whatever the value of the integrand is at $\alpha = n_1$, the new integrand in the corresponding point is zero. If there are any peaks near $\alpha = n_1$, they disappear in the splitting and change of variables. Fig. 11 shows the integrand of $\mathcal{T}_p^{(8)}$, and we see that there are strong peaks in both the real and the imaginary parts near the index of refraction. Figs. 12 and 13 show the integrands for the traveling and evanescent parts in the $u$ representation, and indeed these functions vanish at $u = 0$. Fig. 14 shows the auxiliary function $T_p^{(8)}$. It appears that the results for the $\alpha$ integration and the $u$ integration are identical, so there are no issues as in Fig. 5. However, the runtime for the $\alpha$ integration is 6 min, whereas the integration time in the $u$ domain

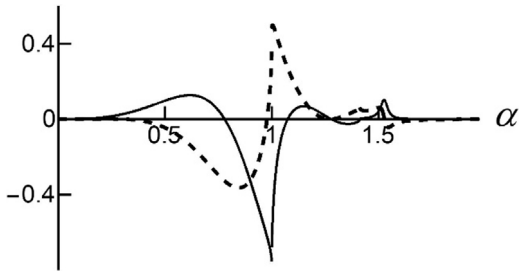


**Fig. 11.** Shown are the real (solid curve) and imaginary (dashed curve) parts of the integrand of $\mathcal{T}_p^{(8)}$ as a function of $\alpha$. The parameter for the layer system are $\varepsilon_1 = 1$, $\varepsilon_2 = 4 + 0.1 * i$, $\varepsilon_3 = 2$, $\mu_1 = \mu_2 = \mu_3 = 1$, $\ell = 4$, $h = 2$, $\overline{\rho} = 3$ and $\overline{z} = 6$. The peak near $\alpha = 1$ is here not due to a $1/v_1$ singularity.

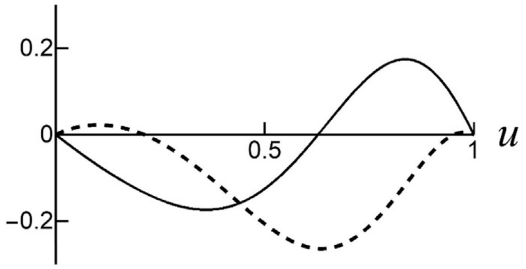


**Fig. 12.** The graph shows the integrand of the traveling part of the function $\mathcal{T}_p^{(8)}$ as a function of $u$.

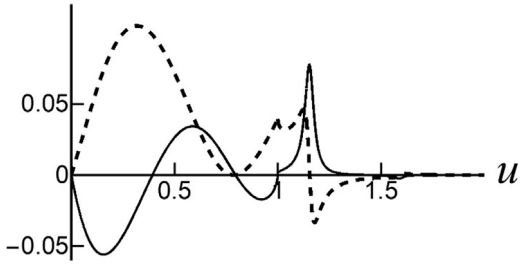


**Fig. 13.** The graph shows the integrand of the evanescent part of the function $\mathcal{T}_p^{(8)}$ as a function of $u$.

is only 2 min. Even though there may be no issues with a singular point, there still is definitely an advantage to split the remaining integrals into their traveling and evanescent parts.

## 7. Field lines of energy flow

An interesting application of the solution with Sommerfeld-type integrals is the visualization of the flow lines of energy. Electromagnetic energy flows along the field lines of the (time averaged) Poynting vector, defined as

$$\mathbf{S}(\mathbf{r})_k = \frac{1}{2\mu_o}\mathrm{Re}\left[\frac{1}{\mu_k}\mathbf{E}(\mathbf{r})_k^* \times \mathbf{B}(\mathbf{r})_k\right]. \tag{31}$$

Here, $k = 1, 2, 3$, indicates the regions, as in Fig. 1. We set

$$\mathbf{S}(\mathbf{r})_k = \mu_1^2 \frac{\zeta^2}{2\mu_o c}\boldsymbol{\sigma}(\mathbf{r})_k, \tag{32}$$

and this defines the dimensionless Poynting vector $\boldsymbol{\sigma}_k$. We then have

$$\boldsymbol{\sigma}(\mathbf{r})_k = \mathrm{Re}\left[\tilde{\mathbf{E}}(\mathbf{r})_k^* \times \tilde{\mathbf{B}}(\mathbf{r})_k\right], \tag{33}$$

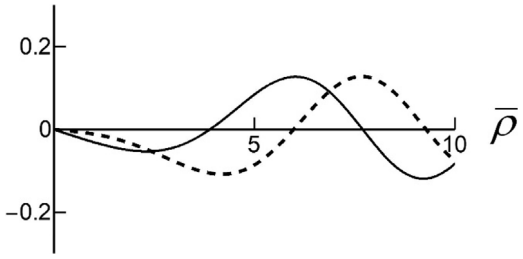


**Fig. 14.** The graph shows the function $\mathcal{T}_p^{(8)}$ as a function of $\overline{\rho}$, for $\overline{z} = 6$. The parameters are the same as for Fig. 11.

in terms of the dimensionless complex field amplitudes, given by Eqs. (15)–(20).

Field lines of energy flow are in general 3D curves, which makes a visualization cumbersome. We shall consider a dipole moment in the $yz$ plane, so that $u_x = 0$. With $u_\phi = 0$, many terms in Eqs. (15)–(20) are zero. It can then be verified from the solution above that for a field point in the $yz$ plane the complex amplitude of the electric field is in the $yz$ plane and the complex amplitude of the magnetic field only has an $x$ component. It then follows that the Poynting vector for a field point in the $yz$ plane is in the $yz$ plane. Therefore, a field line through a point in the $yz$ plane stay in the $yz$ plane, and consequently such a field line is a 2D curve in the $yz$ plane.

A typical example of a flow line diagram is shown in Fig. 15. The parameters are given in the caption. The field lines emanate from the location of the dipole. At the first interface, they bend towards the normal upon crossing, as expected for transition into a denser medium. At the second interface they bend away from the normal, as would optical rays when passing into a thinner medium. For a linear dipole in free space, the field lines would be straight, running outward in the radial direction. It seems from the figure that at the interfaces the field lines smoothly cross the interfaces. This due to the fact that *Mathematica* connects the field lines in the various regions as smooth curves. An enlargement of a crossing point would show that the field lines actually have an abrupt change of direction upon crossing, just like optical rays do upon refraction. Despite the large number of auxiliary functions that need to be computed to make the graph in Fig. 15, the runtime is only 6 min.

Fig. 16 shows the flow line pattern for a counterclockwise rotating dipole moment near a single interface. Vector $\hat{\mathbf{u}}$ is given by Eq. (6). The field lines spiral out of the dipole in a counterclockwise direction, and at the interface they bend towards the normal. Far away, the field lines become approximately straight. The rotation in the flow field is a near field phenomenon that does not extend into the far field. There is a difference in appearance of the field lines in Figs. 15 and 16. For the first figure, we use StreamPoints. Specific points in the $yz$ plane are chosen, and *Mathematica* calculates the field lines through the given points. A high density of field lines implies a stronger field. In Fig. 16, the choice of StreamPoints is left to *Mathematica*. In Fig. 15, all field lines start at the dipole and then run away until they hit the boundary of the graph. In Fig. 16, field lines are broken when they come too close together. This gives a more uniform density of field lines. Both types of graphs are useful. A third possibility (not shown here) is to choose StreamPoints, but then let Mathematica decide which field lines to break in order to give a more uniform density.

Fig. 17 shows the energy flow pattern for a dipole oscillating under 30° with the positive $z$ axis. Most field lines are almost straight, except into the direction of the dipole axis there seems to be turbulence in the energy flow field. An enlargement, as

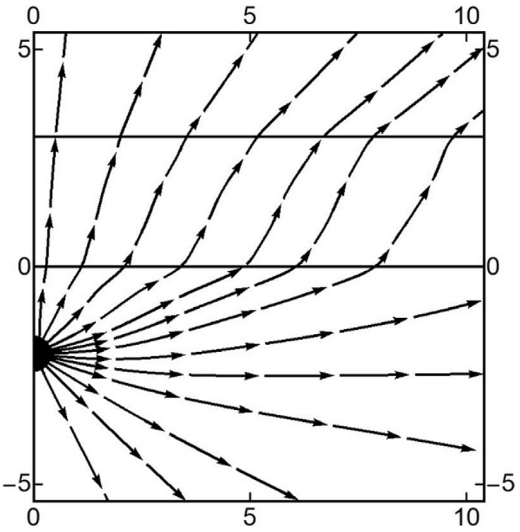


**Fig. 15.** The graph shows the energy flow pattern for radiation emitted by a vertical dipole ($\hat{\mathbf{u}} = \mathbf{e}_z$). The interfaces are located at $\overline{z} = 0$ and $\overline{z} = 3$, indicated by horizontal lines in the figures. The material parameters are $\varepsilon_1 = 1$, $\varepsilon_2 = 4 + 0.01 * i$, $\varepsilon_3 = 2$, $\mu_1 = \mu_2 = \mu_3 = 1$, and the dipole is located at a distance $h = 2$ below the first interface.

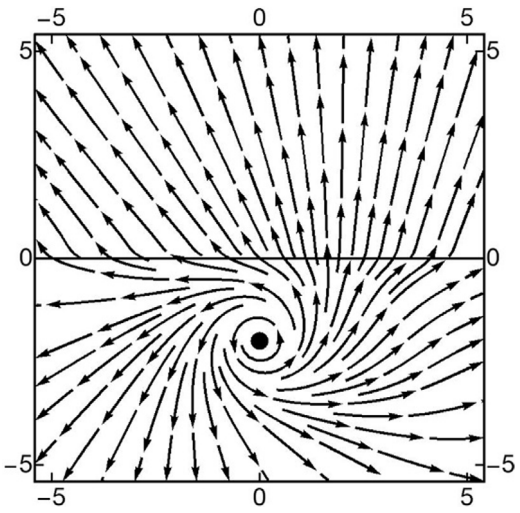


**Fig. 16.** Shown is the energy flow pattern for radiation emitted by a rotating dipole moment near a single interface. The material parameters are $\varepsilon_1 = 1$, $\varepsilon_3 = 4 + 0.01 * i$, $\mu_1 = \mu_3 = 1$, and the dipole is located at a distance $h = 2$ below the interface.

shown in Fig. 18, reveals that this turbulence is actually a string of vortices, located along the dipole axis, and from the location of the dipole to the interface. Each vortex counterrotates the previous one, and in between is a host of singularities. At such points, the direction of the flow field is undetermined, and the Poynting vector is zero.

Another interesting phenomenon can be seen in the top-right part of Fig. 18. Field lines entering the picture on the left cross the interface, and bend away from the normal upon crossing. They bend so much that on the right they re-enter the lower medium, and eventually exit the picture to the right. Such peculiar behavior is a near-field effect that can only be found from the exact solutions of Maxwell's equations, and by considering a very fine scale.

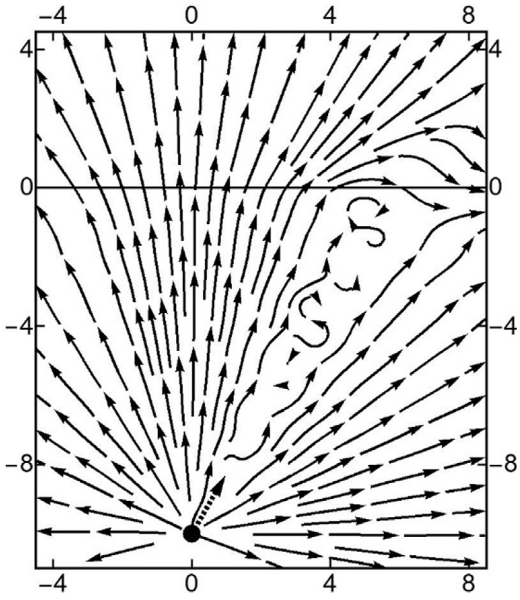


**Fig. 17.** Shown is the energy flow pattern for radiation emitted by a dipole moment oscillating under 30° with the $z$ axis. The material parameters are $\varepsilon_1 = 4$, $\varepsilon_3 = 1 + 0.01 * i$, $\mu_1 = \mu_3 = 1$, and the dipole is located at a distance $h = 10$ below the interface.

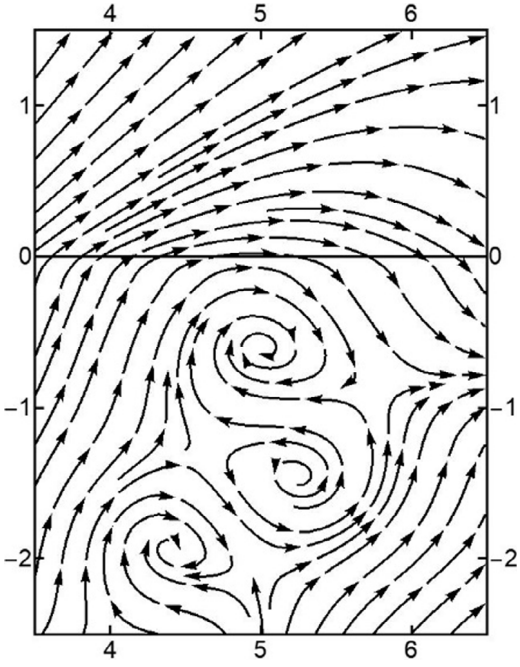


**Fig. 18.** The diagram shows an enlargement of a part of the graph in Fig. 17.

## 8. The programs

The program CPiP-Auxiliary-1.nb computes the auxiliary functions for the layer problem. The material parameters are $\varepsilon_1$, $\mu_1$, $\varepsilon_2$, $\mu_2$, $\varepsilon_3$ and $\mu_3$, which are complex in general. Their imaginary parts must be positive or zero. The values of $\varepsilon_1$ and $\mu_1$ are restricted to positive numbers, necessary for the splitting of the integrals in their traveling and evanescent parts. The dimensionless layer thickness is $\ell$ and the dimensionless distance between the dipole and the lower interface is $h$, and both must be positive. The dimensionless spatial coordinates are $\overline{\rho}$ (positive or zero) and $\overline{z}$ (real). For a given auxiliary function, the value of $\overline{z}$ has to be in

the appropriate range (negative for an $\mathcal{R}$, in between zero and $\ell$ for an $\mathcal{L}$ and larger than $\ell$ for a $\mathcal{T}$). The AccuracyGoal parameter (*ag*) specifies the accuracy for the numerical integration. The best choice seems to be $ag = 6$, although this sometimes leads to non-converging warnings by *Mathematica*. The result is still more than adequate for graphing purposes, and can be ignored. When lowering *ag* to, say, 2, the warnings disappear, but the results are not always reliable. The program graphs an auxiliary function as a function of $\overline{\rho}$ for a given $\overline{z}$, but the main purpose of the program is to provide code for the computation of these functions. This can be copied and pasted into a program that needs these functions. The program CPiP-Auxiliary-2.nb is a simplified version for a single interface. We set $\ell = 0$ in the associated functions, and the $\mathcal{L}$ functions disappear. The main difference is that the Fresnel reflection and transmission coefficients simplify, as shown in the Appendix. The resulting program is much faster than CPiP-Auxiliary-1.nb.

The program CPiP-Field lines-1.nb, and its single interface version CPiP-Field lines 2.nb, generates a streamline picture for the flow of energy in the *yz* plane. The dipole moment has to be taken to be in the *yz* plane, so it has the form $\{0, d_y, d_z\}$ in *Mathematica* notation. The numbers $d_y$ and $d_z$ are arbitrary complex numbers. The normalization as given by Eq. (5) is then done by the program. Alternatively, for a linear dipole the direction $\gamma$ of the dipole axis can be specified. The dipole then oscillates under angle $\gamma$ with the positive $z$ axis. For this case the unit polarization vector of the dipole moment is $\hat{\mathbf{u}} = \{0, \sin\gamma, \cos\gamma\}$. When the variable *gammatf* is set to True, this $\hat{\mathbf{u}}$ will be used, and this vector will be represented by a dashed arrow in the field line figure. If $d_y$ and $d_z$ are to be used, this parameter should be set to False. The parameter *nstep* determines the number of points generated to make the Table for the computation of the field lines with *ListStreamPlot*. A good value seems to be *nstep* = 25. Larger values significantly increase the computation time, but with little or no improvement of the resulting graph. The Poynting vector diverges at the location of the dipole, and this may give numerical problems in the computation of field lines. Since field lines are determined by the direction of the vector field at each point, the vector field can be multiplied through by any positive function. We multiply $\boldsymbol{\sigma}$ by $q_1^5$, and here

$$q_1 = \sqrt{\overline{y}^2 + (\overline{z} + h)^2}, \tag{34}$$

is the dimensionless distance between the field point (in the *yz* plane) and the dipole.

## 9. Conclusions

We have presented a method for the numerical computation of Sommerfeld-type integrals. These integrals are needed for the study of near-field phenomena in electric dipole radiation near an interface. The reflected fields, the transmitted fields and the fields in the layer are expressed in terms of these integrals, and an accurate and efficient method is needed for the computation of these integrals. We have shown that there is a great advantage in splitting the integrals in their traveling and evanescent contributions. On one hand, this eliminates a singularity which is inherent in angular spectra, and on the other hand it improves the accuracy of computation. We have illustrated the feasibility of our approach by applying the technique to make electromagnetic energy flow diagrams in the near field. Very small details, like singularities and sub-wavelength vortices, are perfectly resolved. Even though such diagrams involve the computation of huge numbers of integrals, the computation time for one field line picture remains reasonable (about 15 min, but this depends heavily on the choice of parameters).

## Declaration of competing interest

The authors declare that they have no known competing financial interests or personal relationships that could have appeared to influence the work reported in this paper.

## Appendix

The auxiliary functions for the r, a, b and t waves are constructed as follows. The Fresnel coefficients for plane waves are functions of $\alpha$, given by

*s waves*

$$\Lambda_s(\alpha) = (\mu_2 v_1 + \mu_1 v_2)(\mu_3 v_2 + \mu_2 v_3) + (\mu_2 v_1 - \mu_1 v_2) \times (\mu_3 v_2 - \mu_2 v_3) e^{2iv_2\ell}, \tag{A.1}$$

$$R_s(\alpha) = \frac{1}{\Lambda_s}\left[(\mu_2 v_1 - \mu_1 v_2)(\mu_3 v_2 + \mu_2 v_3) + (\mu_2 v_1 + \mu_1 v_2) \times (\mu_3 v_2 - \mu_2 v_3) e^{2iv_2\ell}\right], \tag{A.2}$$

$$A_s(\alpha) = \frac{2}{\Lambda_s}\mu_2 v_1(\mu_3 v_2 + \mu_2 v_3), \tag{A.3}$$

$$B_s(\alpha) = \frac{2}{\Lambda_s}\mu_2 v_1(\mu_3 v_2 - \mu_2 v_3) e^{iv_2\ell}, \tag{A.4}$$

$$T_s(\alpha) = \frac{4}{\Lambda_s}\mu_2\mu_3 v_1 v_2 e^{iv_2\ell}. \tag{A.5}$$

*p waves*

$$\Lambda_p(\alpha) = (\varepsilon_2 v_1 + \varepsilon_1 v_2)(\varepsilon_3 v_2 + \varepsilon_2 v_3) + (\varepsilon_2 v_1 - \varepsilon_1 v_2) \times (\varepsilon_3 v_2 - \varepsilon_2 v_3) e^{2iv_2\ell}, \tag{A.6}$$

$$R_p(\alpha) = \frac{1}{\Lambda_p}\left[(\varepsilon_2 v_1 - \varepsilon_1 v_2)(\varepsilon_3 v_2 + \varepsilon_2 v_3) + (\varepsilon_2 v_1 + \varepsilon_1 v_2) \times (\varepsilon_3 v_2 - \varepsilon_2 v_3) e^{2iv_2\ell}\right], \tag{A.7}$$

$$A_p(\alpha) = \frac{2}{\Lambda_p}\frac{n_2}{n_1}\varepsilon_1 v_1(\varepsilon_3 v_2 + \varepsilon_2 v_3), \tag{A.8}$$

$$B_p(\alpha) = \frac{2}{\Lambda_p}\frac{n_2}{n_1}\varepsilon_1 v_1(\varepsilon_3 v_2 - \varepsilon_2 v_3) e^{iv_2\ell}, \tag{A.9}$$

$$T_p(\alpha) = \frac{4}{\Lambda_p}\frac{n_3}{n_1}\varepsilon_1\varepsilon_2 v_1 v_2 e^{iv_2\ell}. \tag{A.10}$$

In angular spectra representations, the integrands have a factor $\alpha/v_1$. For $n_1 > 0$, this gives a singularity on the integration axis, since $v_1 = 0$ at $\alpha = n_1$. All Fresnel coefficients, except the ones for r waves, have a factor $v_1$. Therefore, we define reduced Fresnel coefficients as

$$A'_\sigma(\alpha) = A_\sigma / v_1, \tag{A.11}$$

$$B'_\sigma(\alpha) = B_\sigma / v_1, \tag{A.12}$$

$$T'_\sigma(\alpha) = T_\sigma / v_1, \tag{A.13}$$

for $\sigma = s, p$. In this way, most of the singularities cancel out.

The associated functions are functions of $\alpha$ and $\overline{z}$, defined as

$$r_\sigma(\alpha, \overline{z}) = R_\sigma e^{iv_1(h-\overline{z})}, \tag{A.14}$$

$$a_\sigma(\alpha, \overline{z}) = A'_\sigma e^{iv_1 h + iv_2\overline{z}}, \tag{A.15}$$

$$b_\sigma(\alpha, \overline{z}) = B'_\sigma e^{iv_1 h + iv_2(\ell-\overline{z})}, \tag{A.16}$$

$$t_\sigma(\alpha, \overline{z}) = T'_\sigma e^{iv_1 h + iv_3(\overline{z}-\ell)}, \tag{A.17}$$

for $\sigma = s, p$.

The auxiliary functions that enter the expressions for the electric and magnetic fields are functions of the coordinates $\overline{\rho}$ and $\overline{z}$. They are defined as

*s waves*

$$\mathcal{R}_s^{(1)}(\overline{\rho},\overline{z}) = \frac{i}{2}\int_0^\infty d\alpha\,\frac{\alpha}{v_1} r_s (J_0 + J_2), \tag{A.18}$$

$$\mathcal{R}_s^{(2)}(\overline{\rho},\overline{z}) = \frac{i}{2}\int_0^\infty d\alpha\,\frac{\alpha}{v_1} r_s (J_0 - J_2), \tag{A.19}$$

$$\mathcal{R}_s^{(3)}(\overline{\rho},\overline{z}) = \frac{i}{2}\int_0^\infty d\alpha\,\alpha\, r_s v_1 (J_0 - J_2), \tag{A.20}$$

$$\mathcal{R}_s^{(4)}(\overline{\rho},\overline{z}) = -\frac{i}{2}\int_0^\infty d\alpha\,\alpha\, r_s v_1 (J_0 + J_2), \tag{A.21}$$

$$\mathcal{R}_s^{(5)}(\overline{\rho},\overline{z}) = -\int_0^\infty d\alpha\,\frac{\alpha}{v_1} r_s \alpha J_1, \tag{A.22}$$

$$\mathcal{L}_s^{(1)}(\overline{\rho},\overline{z}) = \frac{i}{2}\int_0^\infty d\alpha\,\alpha (a_s + b_s)(J_0 + J_2), \tag{A.23}$$

$$\mathcal{L}_s^{(2)}(\overline{\rho},\overline{z}) = \frac{i}{2}\int_0^\infty d\alpha\,\alpha (a_s + b_s)(J_0 - J_2), \tag{A.24}$$

$$\mathcal{L}_s^{(3)}(\overline{\rho},\overline{z}) = -\frac{i}{2}\int_0^\infty d\alpha\,\alpha (a_s - b_s) v_2 (J_0 - J_2), \tag{A.25}$$

$$\mathcal{L}_s^{(4)}(\overline{\rho},\overline{z}) = \frac{i}{2}\int_0^\infty d\alpha\,\alpha (a_s - b_s) v_2 (J_0 + J_2), \tag{A.26}$$

$$\mathcal{L}_s^{(5)}(\overline{\rho},\overline{z}) = -\int_0^\infty d\alpha\,\alpha (a_s + b_s)\alpha J_1, \tag{A.27}$$

$$\mathcal{T}_s^{(1)}(\overline{\rho},\overline{z}) = \frac{i}{2}\int_0^\infty d\alpha\,\alpha\, t_s (J_0 + J_2), \tag{A.28}$$

$$\mathcal{T}_s^{(2)}(\overline{\rho},\overline{z}) = \frac{i}{2}\int_0^\infty d\alpha\,\alpha\, t_s (J_0 - J_2), \tag{A.29}$$

$$\mathcal{T}_s^{(3)}(\overline{\rho},\overline{z}) = -\frac{i}{2}\int_0^\infty d\alpha\,\alpha\, t_s v_3 (J_0 - J_2), \tag{A.30}$$

$$\mathcal{T}_s^{(4)}(\overline{\rho},\overline{z}) = \frac{i}{2}\int_0^\infty d\alpha\,\alpha\, t_s v_3 (J_0 + J_2), \tag{A.31}$$

$$\mathcal{T}_s^{(5)}(\overline{\rho},\overline{z}) = -\int_0^\infty d\alpha\,\alpha\, t_s \alpha J_1. \tag{A.32}$$

*p waves*

$$\mathcal{R}_p^{(1)}(\overline{\rho},\overline{z}) = -\frac{i}{2n_1^2}\int_0^\infty d\alpha\,\alpha\, r_p v_1 (J_0 - J_2), \tag{A.33}$$

$$\mathcal{R}_p^{(2)}(\overline{\rho},\overline{z}) = -\frac{i}{2n_1^2}\int_0^\infty d\alpha\,\alpha\, r_p v_1 (J_0 + J_2), \tag{A.34}$$

$$\mathcal{R}_p^{(3)}(\overline{\rho},\overline{z}) = \frac{i}{n_1^2}\int_0^\infty d\alpha\,\frac{\alpha}{v_1} r_p \alpha^2 J_0, \tag{A.35}$$

$$\mathcal{R}_p^{(4)}(\overline{\rho},\overline{z}) = -\frac{1}{n_1^2}\int_0^\infty d\alpha\,\alpha\, r_p \alpha J_1, \tag{A.36}$$

$$\mathcal{R}_p^{(5)}(\overline{\rho},\overline{z}) = -\frac{i}{2}\int_0^\infty d\alpha\,\alpha\, r_p (J_0 + J_2), \tag{A.37}$$

$$\mathcal{R}_p^{(6)}(\overline{\rho},\overline{z}) = \frac{i}{2}\int_0^\infty d\alpha\,\alpha\, r_p (J_0 - J_2), \tag{A.38}$$

$$\mathcal{R}_p^{(7)}(\overline{\rho},\overline{z}) = \int_0^\infty d\alpha\,\frac{\alpha}{v_1} r_p \alpha J_1, \tag{A.39}$$

$$\mathcal{L}_p^{(1)}(\overline{\rho},\overline{z}) = \frac{i}{2n_1 n_2}\int_0^\infty d\alpha\,\alpha (a_p - b_p) v_1 v_2 (J_0 - J_2), \tag{A.40}$$

$$\mathcal{L}_p^{(2)}(\overline{\rho},\overline{z}) = \frac{i}{2n_1 n_2}\int_0^\infty d\alpha\,\alpha (a_p - b_p) v_1 v_2 (J_0 + J_2), \tag{A.41}$$

$$\mathcal{L}_p^{(3)}(\overline{\rho},\overline{z}) = \frac{i}{n_1 n_2}\int_0^\infty d\alpha\,\alpha (a_p + b_p)\alpha^2 J_0, \tag{A.42}$$

$$\mathcal{L}_p^{(4)}(\overline{\rho},\overline{z}) = \frac{1}{n_1 n_2}\int_0^\infty d\alpha\,\alpha (a_p - b_p)\alpha v_2 J_1, \tag{A.43}$$

$$\mathcal{L}_p^{(5)}(\overline{\rho},\overline{z}) = \frac{1}{n_1 n_2}\int_0^\infty d\alpha\,\alpha (a_p + b_p)\alpha v_1 J_1, \tag{A.44}$$

$$\mathcal{L}_p^{(6)}(\overline{\rho},\overline{z}) = -\frac{in_2}{2n_1}\int_0^\infty d\alpha\,\alpha (a_p + b_p) v_1 (J_0 + J_2), \tag{A.45}$$

$$\mathcal{L}_p^{(7)}(\overline{\rho},\overline{z}) = \frac{in_2}{2n_1}\int_0^\infty d\alpha\,\alpha (a_p + b_p) v_1 (J_0 - J_2), \tag{A.46}$$

$$\mathcal{L}_p^{(8)}(\overline{\rho},\overline{z}) = \frac{n_2}{n_1}\int_0^\infty d\alpha\,\alpha (a_p + b_p)\alpha J_1, \tag{A.47}$$

$$\mathcal{T}_p^{(1)}(\overline{\rho},\overline{z}) = \frac{i}{2n_1 n_3}\int_0^\infty d\alpha\,\alpha\, t_p v_1 v_3 (J_0 - J_2), \tag{A.48}$$

$$\mathcal{T}_p^{(2)}(\overline{\rho},\overline{z}) = \frac{i}{2n_1 n_3}\int_0^\infty d\alpha\,\alpha\, t_p v_1 v_3 (J_0 + J_2), \tag{A.49}$$

$$\mathcal{T}_p^{(3)}(\overline{\rho},\overline{z}) = \frac{i}{n_1 n_3}\int_0^\infty d\alpha\,\alpha\, t_p \alpha^2 J_0, \tag{A.50}$$

$$\mathcal{T}_p^{(4)}(\overline{\rho},\overline{z}) = \frac{1}{n_1 n_3}\int_0^\infty d\alpha\,\alpha\, t_p \alpha v_3 J_1, \tag{A.51}$$

$$\mathcal{T}_p^{(5)}(\overline{\rho},\overline{z}) = \frac{1}{n_1 n_3}\int_0^\infty d\alpha\,\alpha\, t_p \alpha v_1 J_1, \tag{A.52}$$

$$\mathcal{T}_p^{(6)}(\overline{\rho},\overline{z}) = -\frac{in_3}{2n_1}\int_0^\infty d\alpha\,\alpha\, t_p v_1 (J_0 + J_2), \tag{A.53}$$

$$\mathcal{T}_p^{(7)}(\overline{\rho},\overline{z}) = \frac{in_3}{2n_1}\int_0^\infty d\alpha\,\alpha\, t_p v_1 (J_0 - J_2), \tag{A.54}$$

$$\mathcal{T}_p^{(8)}(\overline{\rho},\overline{z}) = \frac{n_3}{n_1}\int_0^\infty d\alpha\,\alpha\, t_p \alpha J_1. \tag{A.55}$$

Here, the argument of each Bessel function is $J_k = J_k(\alpha\overline{\rho})$, needed for $k = 0$, 1, and 2.

It should be noted that as compared to Ref. [24], there is a slight improvement in the presentation. In Ref. [24], the a and b waves were constructed separately, with their own auxiliary functions, and then the a and b waves were added in the expressions for the fields. It has come to our attention that this is an unnecessary complication. We have now added the a and b waves at the level of the auxiliary functions, and introduced the $\mathcal{L}_\sigma^{(i)}$ functions. This reduces the number of auxiliary functions from 51 to 38.

For the case of a single interface, we set $\ell = 0$. Then we do not need the functions $\mathcal{L}_\sigma^{(i)}$. We set $\ell = 0$ in the associated functions, and the remaining Fresnel coefficients simplify to

$$R_s = \frac{\mu_3 v_1 - \mu_1 v_3}{\mu_3 v_1 + \mu_1 v_3}, \tag{A.56}$$

$$T_s = \frac{2\mu_3 v_1}{\mu_3 v_1 + \mu_1 v_3}, \tag{A.57}$$

$$R_p = \frac{\varepsilon_3 v_1 - \varepsilon_1 v_3}{\varepsilon_3 v_1 + \varepsilon_1 v_3}, \tag{A.58}$$

$$T_p = \frac{n_3}{n_1}\frac{2\varepsilon_1 v_1}{\varepsilon_3 v_1 + \varepsilon_1 v_3}. \tag{A.59}$$

## References


[1] A. Sommerfeld, Ann. der Physik 28 (1909) 665-736.
[2] M. Siegel, R.W.P. King, J. Appl. Phys. 41 (1970) 2415–2423.
[3] P. Parhami, Y. Rahmat-Samii, R. Mittra, IEEE Trans. Antennas Propag. AP-28 (1980) 100–104.
[4] Y. Rahmat-Samii, R. Mittra, P. Parhami, Electromagnetics 1 (1981) 1–28.
[5] R.W.P. King, J. Appl. Phys. 53 (1982) 8476–8482.
[6] W.A. Johnson, D.G. Dudley, Radio Sci. 18 (1983) 175–186.
[7] M. Paulus, P. Gay-Balmaz, O.J.F. Martin, Phys. Rev. E 62 (2000) 5797–5807.
[8] K. Sarabandi, M.D. Casciato, Il-S. Koh, IEEE Trans. Antennas Propag. 50 (2002) 1222–1235.
[9] W. Lukosz, R.E. Kunz, J. Opt. Soc. Amer. 67 (1977) 1607–1615.
[10] R.R. Chance, A. Prock, R. Silbey, Adv. Chem. Phys. 39 (1978) 1–65.
[11] J.E. Sipe, Surf. Sci. 105 (1981) 489–504.
[12] J.B. Pendry, Phys. Rev. Lett. 85 (2000) 3966–3969.
[13] J.A. Girón-Sedas, J.R. Mejía-Salazar, J.C. Granade, O.N. Oliveira, Phys. Rev. B 94 (2016) 245430(5).
[14] F.J. Rodríguez-Fortuño, M.F. Picardi, A.V. Zayats, Phys. Rev. B 97 (2018) 205401(9).
[15] F.J. Rodríguez-Fortuño, A. Vakil, N. Engheta, Phys. Rev. Lett. 112 (2014) 033902(5).
[16] H.F. Arnoldus, Z. Xu, J. Opt. Soc. Amer. B 36 (2019) F18–F24.
[17] M.J.O. Strutt, Ann. Phys. 393 (1929) 721–750.
[18] W. Lukosz, R.E. Kunz, J. Opt. Soc. Amer. 67 (1977) 1615–1619.
[19] H.F. Arnoldus, J.T. Foley, J. Opt. Soc. Amer. A 21 (2004) 1109–1117.
[20] A.J. Yuffa, J.A. Scales, J. Comput. Phys. 231 (2012) 4823–4834.
[21] H.F. Arnoldus, Adv. Imaging Electron Phys. 132 (2004) 1–67.
[22] I.V. Lindell, Methods for Electromagnetic Field Analysis (Oxford, 1992), Section 1.4.
[23] J.D. Jackson, Classical Electrodynamics, third ed., Wiley, New York, p. 411.
[24] H.F. Arnoldus, M.J. Berg, J. Modern Opt. 62 (2015) 218–288, in the online version (page numbers in the printed version are 244-245).